Communication

Asymmetrically Layered Unit Cell Topology to Reduce Cell Gap of Liquid Crystals for 5G Millimeter-Wave Transmissive Reconfigurable Intelligent Surface Applications

Jaehoon Kim, Jun Hwa Oh, Sang-Hyuk Wi, Jungsuek Oh

***Abstract*— This study presents transmissive reconfigurable intelligent surface (TRIS) unit cells (UCs) with slimmed liquid crystals (LCs), where the effective cell gap is electromagnetically tailored to control the LC using empirically practical voltage values. Prior LC-based transmissive UCs utilize thickened cell gaps at millimeter-wave frequencies due to limited parametric degrees of freedom, aiming for enhanced performance, but this approach is unfavorable in terms of LC controllability. Therefore, a coupled resonator-loaded UC featuring a dumbbell-shaped complementary loop with intrinsically reduced coupling strength is proposed, despite the close proximity due to the slimmed cell gap. Moreover, a cleverly designed asymmetrical topology is proposed, where the resonators are positioned apart from each other in the perpendicular direction of the coupled dominant current. The designed UC achieves a simulated phase tuning range (PTR) of 123° by employing only a single-layered LC with a cell gap of 0.21 mm, which is improved more than two times than that of the previously studied counterpart. In addition, an operating range of 27.9–29 GHz with reasonable loss sustainable for entire range of LC dielectric constant is attained successfully, contrary to previous works where low loss is maintained only for a single tone (ST) frequency.**

***Index Terms*— Cell gap, coupling, liquid crystal (LC), transmissive reconfigurable intelligent surface (TRIS).**

I. Introduction

The millimeter-wave (mmWave) frequency has been commercialized for 5G due to the demand for high-speed and low-latency wireless communications; however, many wireless network operators face challenges in providing affordable services to users due to the narrowed coverage caused by the abrupt increase in high-frequency loss. Therefore, the sub-6 GHz band is unintentionally utilized as the primary frequency band, and the 3GPP defines various use cases as part of a transitional process to effectively disseminate advanced quality. Among the various cases defined, reconfigurable intelligent surfaces (RISs) have been evaluated as a core technology for next-generation communication. The RIS relays arbitrary signals in a manner that spatially controls the wavefront of the incident waves and has the potential for economic popularization. Among the reconfigurable components, liquid crystals (LCs) are actively chosen for RIS over other candidates due to their operability at high frequencies with a reasonable loss. However, research on LC-based RIS is primarily limited to the reflective type rather than the transmissive type [1], [2], [3], [4], [5]. This limitation arises from the technical challenge of achieving a shared frequency band where high transmittance is preserved despite fluctuations in the LC dielectric constant (ε_{LC}) and simultaneously achieving a practical phase tuning range (PTR) within that band.

Despite these challenging issues, several studies attempted to design unit cells (UCs) for LC-based transmissive RISs (TRIS) in mmWave [6], [7], [8], [9]. In [6] and [7], a dual-layered LC was utilized, which is not favored for fabrication, to address the issues of loss and PTR. Moreover, LC heights (cell gap) of 0.58 and 0.762 mm were utilized, which cannot be controlled empirically with practical voltage values. Generally, the cell gap was confined to less than 0.3 mm in microwave to be fully controlled with dc voltages under 30 V [10], [11], [12], [13], [14]. In [15], a dc potential difference of 400 V was applied to the electrodes to control the cell gap of 0.5 mm, which is unfavorable for practical feasibility. In [8], a UC utilizing a single-layered LC with a feasible cell gap of 0.015 mm was reported. However, low loss was maintained only at a single tone (ST), and a narrow PTR of 60° was achieved. In the terahertz (THz) band, several slimmed cell gaps were reported, as the cell gap can be reduced in inverse proportion to the frequency [16], [17], [18], [19]. However, low loss was sustained only at a ST, and reasonable properties and experimental results were rarely reported.

Thus, this study proposes an asymmetrically layered UC topology that employs a single-layered LC with a slimmed cell gap that can be controlled using empirically practical voltage values, while preserving improved transmissive performance for mmWave applications. The main contributions of this study are summarized as follows:

1) A novel asymmetrical offset topology is successfully developed for slimmed LC in mmWave applications where the reduction of the cell gap is limited compared to higher frequencies.
2) The skillfully designed resonator achieves a smaller offset value while preserving the UC period and dc electrode size flexibility and meeting the minimal PCB etching process feature size.
3) The first transmissive UC with a fully controlled, slimmed LC achieves improved loss and PTR, even with a wider bandwidth.

The remainder of the communication is arranged as follows. Section II presents an LC-based transmissive UC topology. A modified complementary loop-loaded coupled resonator is employed to achieve an operating band with reasonable loss and PTR, which is sustainable even in variations of ε_{LC}. Furthermore, an inventive asymmetrical offset topology that electromagnetically tailors the effective cell gap to improve the transmissive characteristics without thickening the physical cell gap is proposed. Finally, Section III concludes the study.

Manuscript received 22 August 2023; revised 6 November 2023; accepted 28 November 2023. Date of publication 8 December 2023; date of current version 7 March 2024. This work was supported by SAMSUNG Research, Samsung Electronics Company Ltd. *(Corresponding author: Jungsuek Oh.)*

Jaehoon Kim and Jungsuek Oh are with the School of Electrical and Computer Engineering, Institute of New Media and Communications (INMC), Seoul National University, 152-742 Seoul, South Korea (e-mail: jaehoonkim@snu.ac.kr; jungsuek@snu.ac.kr).

Jun Hwa Oh and Sang-Hyuk Wi are with the Samsung Research, 06765 Seoul, South Korea (e-mail: james33.oh@samsung.com; sang-hyuk.wi@samsung.com).

Color versions of one or more figures in this communication are available at https://doi.org/10.1109/TAP.2023.3338863.

Digital Object Identifier 10.1109/TAP.2023.3338863

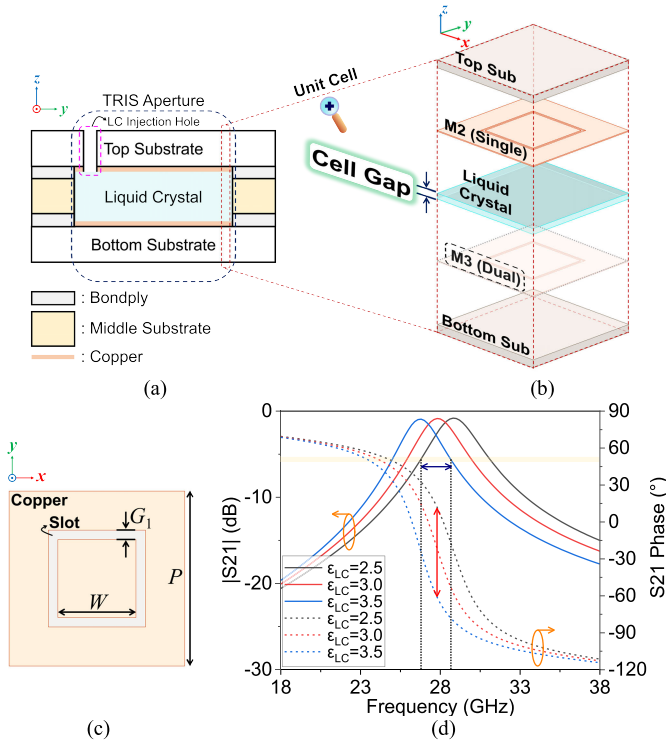

Fig. 1. (a) Side view of an LC-based TRIS. (b) Exploded view of a UC. (c) Top view of a complementary square loop resonator ($P = 4$ mm, $G_1 = 0.1$ mm, $W = 1.7$ mm). (d) Simulated Floquet S_{21} of a single resonator-loaded UC for ε_{LC}.

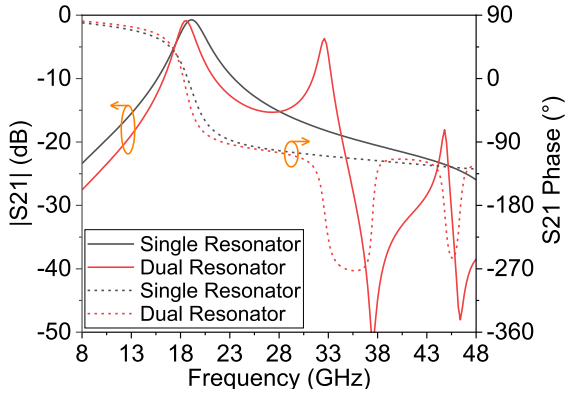

Fig. 2. Simulated S_{21} of single and dual resonator-loaded UCs for $\varepsilon_{LC} = 3.0$.

II. Slimmed LC-Based TRIS UC

A. A Complementary Loop-Loaded Resonator

Fig. 1(a) and (b) show the side view of the LC-based TRIS and the exploded view of a constituent UC. The TRIS has a stacked PCB topology in which the middle substrate is perforated to enclose the LC inside. The top and bottom substrates were bonded to the perforated middle substrate on both sides using a bondply. Subsequently, the LC was injected into the hole in the top substrate and sealed with epoxy. The top and bottom substrates are Rogers RO4350, each having a thickness of 0.25 mm and dielectric constant and loss tangent of 3.66 and 0.004, respectively. The bondply is Rogers 6250, with a thickness of 0.04 mm and dielectric constant and loss tangent of 2.32 and 0.0013, respectively. The middle substrate is Rogers RO4350 with a thickness of 0.13 mm, and a cell gap of 0.21 mm was formed using two layers of bondply. The LC is GT7-29001 from Merck, which has ε_{LC} in the range of 2.5–3.5 and a corresponding loss tangent of 0.0116–0.0064 at 19 GHz. As depicted in Fig. 1(b), the transmissive resonators with up to two metal layers (M2 and M3) can be effectively controlled by altering the ε_{LC} of the adjacent single-layered LC. In this study, a bandpass complementary loop resonator was employed for each metal layer [20]. The single resonator-loaded UC employs only the M2 layer, while the dual resonator-loaded UC, discussed later, utilizes both the M2 and M3 layers. Fig. 1(d) shows the simulated Floquet S_{21} of a single resonator-loaded UC for ε_{LC} and Fig. 1(c) shows the corresponding resonator topology and its design parameters. UCs were analyzed based on Floquet boundary simulation of Ansys High Frequency Structure Simulator (HFSS). The passband is achieved at the resonant frequency and moves toward lower frequencies as ε_{LC} increases. Note that the transmissive UC has minimal loss at its resonant frequency, in contrast to the reflective one that has maximal loss at the resonant frequency [1]. Accordingly, due to the rapid increase in loss as the resonant frequency deviates from the target frequency governed by the equation $|S_{21}| = \cos(\angle S_{21})$, which is generally satisfied in transmissive surfaces regardless of the element shape, maintaining low loss within the desired frequency band while the passband shifts in response to changes in ε_{LC} is highly constrained [21]. Furthermore, if the slope of $\angle S_{21}$ becomes steeper to enhance the PTR, the loss is increased more rapidly, thereby imposing greater constraints on establishing a specific bandwidth for ε_{LC}. Hence, there is a need to establish a new standard for losses in transmissive UCs. From now on, the frequency band where the condition of $|S_{21}| \geq -6$ dB is commonly satisfied for all ε_{LC} is defined as the operating band. This range is indicated by a blue horizontal arrow, while the corresponding PTR, depicted as the red vertical arrow, is also determined. As shown in Fig. 1(d), the single resonator-loaded UC with single-layered LC achieves an insufficient PTR of 70°, in contrast to reflective UCs that achieve a sufficient PTR even with conventional single resonator-loaded topologies [1], [2], [3], [4], [5]. Therefore, a dual resonator-loaded UC with a second-order response that can attain an expanded PTR along with a steeper slope in the phase response according to the increased order of the filter is proposed.

Fig. 2 shows the simulated S_{21} of single and dual resonator-loaded UCs for the median value of the variable ε_{LC} range (3.0) in Fig. 1(b). The dual resonator-loaded UC exhibits virtually independent dual-band resonant frequencies, which are difficult to demonstrate as a higher-order response with a steeper phase gradient due to the substantial divergence between the two resonant frequencies. In the proposed UC topology, the cell gap of the LC is confined to a slimmed 0.21 mm, leading to a close proximity between the two resonators, which inevitably results in mutual coupling components. Therefore, a magnetically coupled equivalent circuit is introduced, as shown in Fig. 3, to analyze the two resonant frequencies that are separated from each other despite the identical physical configuration of the two resonators, where L and C are the self-inductance and self-capacitance, respectively, and L_m is the mutual inductance [22], [23]. In addition to the magnetically coupled effect, which is expressed as an impedance inverter, the self-inductance and self-capacitance in the coupled circuit of the Floquet boundary can be defined as $L = L_0 + L_m$ and $C = C_0 - C_m$, where L_0 and C_0 denote the resonator inductance and capacitance without apertures on the other metal layer in neighboring UCs. This occurs because the adjacent apertures in the other layer increase the resonator inductance and decrease the resonator capacitance [24].

Thus, if the symmetry plane T–T′ in Fig. 3 is replaced by an electric wall (or short-circuit) or magnetic wall (or open-circuit), the

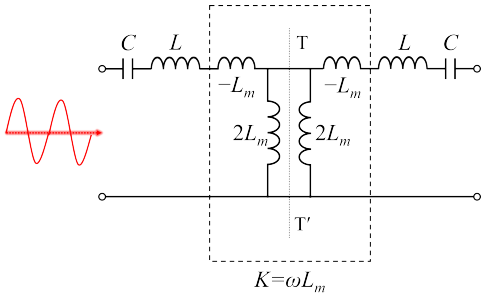

Fig. 3. Equivalent circuit of the proposed coupled resonator-loaded UC with an impedance inverter.

two resonant frequencies of the coupled resonator-loaded UC can be expressed as follows:

$$f_e = \frac{1}{2\pi\sqrt{L_0\,(C_0 - C_m)}} \tag{1}$$

$$f_m = \frac{1}{2\pi\sqrt{(L_0 + 2L_m)\,(C_0 - C_m)}}. \tag{2}$$

According to the equations, the value of f_m is comparable to the resonant frequency of the single resonator-loaded UC, due to the cancellation effect between the $+2L_m$ and $-C_m$ terms in the denominator. However, f_e has an increased resonant frequency due to the reduction in the denominator caused by $-C_m$, which corresponds well to the results in Fig. 2. In conclusion, to obtain a second-order bandpass response at the target frequency by reducing the deviation between the two resonant frequencies, it is necessary to lower the mutual coupling coefficient. The most straightforward approach to reducing the coupling coefficient is increasing the physical cell gap to mitigate field interference between the two resonators. Fig. 4(a) shows the simulated $|S_{21}|$ of the coupled resonator-loaded UCs for $\varepsilon_{\mathrm{LC}} = 3.0$ according to the cell gap. As the cell gap increases, f_e and f_m intentionally move toward the resonant frequency of the single resonator-loaded UC. However, increasing the cell gap is not desirable for optimizing the UC in terms of LC controllability. As shown in Fig. 4(a), in order to achieve the convergence of two resonant frequencies and establish the desired frequency band for the operating band, previously defined as $|\mathrm{S21}| \geq -6$ dB, an excessively large cell gap of over 1 mm is required. Therefore, an alternative design methodology that enables improved transmissive characteristics is required to tailor the effective cell gap of the UC without compromising controllability.

B. Asymmetrical Offset Topology

Herein, we propose a design methodology that successfully obtains an electromagnetically tailored effective cell gap without thickening the physical cell gap. The coupled complementary loop resonators are symmetrically aligned with respect to the central axis within the M2 and M3 layers, as depicted in Fig. 1(b). In contrast, an innovative UC topology wherein the two resonators are strategically positioned apart along the y-direction, perpendicular to the direction of the dominantly coupled current of the x-direction is proposed. Fig. 4(b) shows the simulated $|S_{21}|$ of the coupled resonator-loaded UCs for $\varepsilon_{\mathrm{LC}} = 3.0$ according to offset values of the resonators in the y-direction. It is worth noting that, with an increase in $Offset_y$, which is defined in the same manner as that shown in Fig. 9(a) and (b), f_m moves toward f_e in a distinct manner from the variation in Fig. 4(a). When interpreted by (1) and (2), f_e hardly changes compared to that in Fig. 4(a) as the physical cell gap, which is a dominant factor for C_m, remains unchanged. Conversely, the distance between the x-polarized

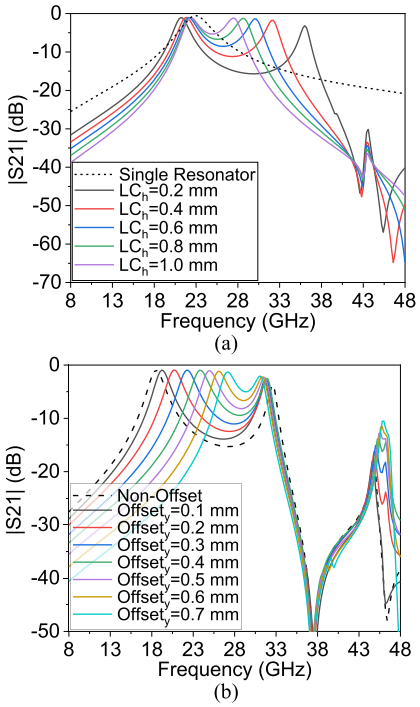

Fig. 4. Simulated $|S_{21}|$ of the coupled resonator-loaded UCs for $\varepsilon_{\mathrm{LC}} = 3.0$ according to (a) cell gap and (b) offset values.

currents, that induce the dominantly coupled magnetic field of each resonator increases effectively. Therefore, L_m decreases, causing f_m to shift toward f_e accordingly. While the electromagnetically increased effective cell gap brings the two resonant frequencies closer, the significant frequency separation stemming from the substantial coupling coefficient necessitates a sizable value of $Offset_y$. In the practical TRIS UC topologies, where each UC is subjected to an individually applied dc voltage, there is a need for electrical isolation through the outer gap of the M2 resonator, as depicted in the purple region of Fig. 9(a). Therefore, a complementary resonator topology in M2 with a large $Offset_y$ could potentially violate the minimum feature size of the standard PCB copper etching process and extend beyond the outer boundary. Furthermore, this limits the design of UCs with smaller periods. Thus, a novel modified dumbbell-shaped loop topology, inherently manipulated with a reduced coupling coefficient even under symmetrical alignment, is proposed, as shown in Fig. 9(a) and (b). Fig. 5 shows the simulated $|S_{21}|$ of the UCs of the non-offset topology for $\varepsilon_{\mathrm{LC}} = 3.0$, with a conventional square loop and a modified loop. Note that the altered design exhibits a diminished coupling coefficient compared to the square counterpart, featuring a significantly narrower gap between the two resonant frequencies. The newly generated transmission zero (TZ) around 14.5 GHz is attributed to the M2 gap for electrical isolation and does not affect the passband characteristics. Fig. 6 shows the simulated $|S_{21}|$ of the modified coupled resonator-loaded UCs according to offset values of the resonators along the y-direction. Note that the successful convergence of the two resonant frequencies is achieved using smaller $Offset_y$ values, which are in contrast to those in Fig. 4(b). As $Offset_y$ increases, an unintended TZ occurs around 25.5 GHz as the electric coupling coefficient increases [23]. Fig. 7 shows the simulated $|S_{21}|$ of the modified coupled resonator-loaded UCs for $Offset_y = 0.3$ mm and $\varepsilon_{\mathrm{LC}} = 3.0$ according to electrical isolation values of M2 electrodes. As G_2 increases, which is defined in the same manner as that shown in Fig. 9(a), the new TZ shifts toward higher frequencies. As TZ approaches the lower resonance, it generates a significant

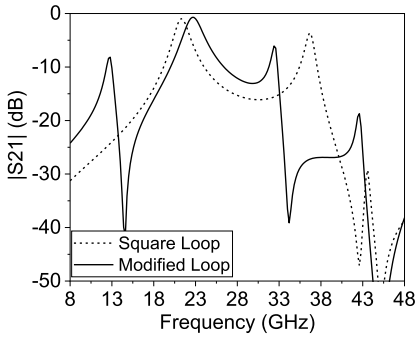

Fig. 5. Simulated $|S_{21}|$ of UCs with non-offset topology for $\varepsilon_{\mathrm{LC}} = 3.0$ using a conventional square loop and a modified loop.

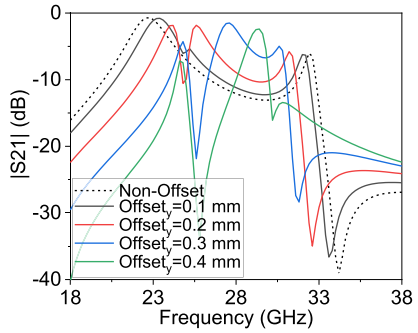

Fig. 6. Simulated $|S_{21}|$ of the modified coupled resonator-loaded UCs for $\varepsilon_{\mathrm{LC}} = 3.0$ according to offset values of resonators along the y-direction.

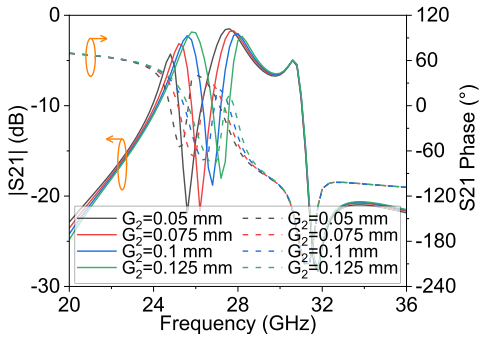

Fig. 7. Simulated $|S_{21}|$ of the modified coupled resonator-loaded UCs for $Offset_y = 0.3$ mm and $\varepsilon_{\mathrm{LC}} = 3.0$ according to electrical isolation values of M2 electrodes.

gradient in the $|S_{21}|$ response of the lower skirt, resulting in a sharper gradient in $\angle S_{21}$. This approach can serve as a methodology to optimize PTR without controlling $Offset_y$, but it does introduce an inherent trade-off by narrowing the bandwidth, necessitating an advanced compromise. Fig. 8 shows the S_{21} of the modified coupled resonator-loaded UCs with offset topology according to $\varepsilon_{\mathrm{LC}}$ with 3 and 6 dB losses for ST operation. In the proposed topology, a PTR of 120° is achieved with $|S_{21}| \geq -3$ dB, and a PTR of 170° is achieved with $|S_{21}| \geq -6$ dB. For a broader bandwidth, the operating band can be extended by adjusting the $Offset_y$ or G_2 value. However, note that such adjustments can lead to a decrease in PTR, as specified by the governing equation. Furthermore, as the $Offset_y$ decreases, the linearity of the phase response deteriorates, resulting in an increased error in the phase change for the same $\varepsilon_{\mathrm{LC}}$ variation within the operating band.

Fig. 9(a) and (b) show the final configuration of the coupled resonators of the proposed UC, and Table I shows the corresponding design parameters and their values. An $Offset_y$ value of 0.3 mm is

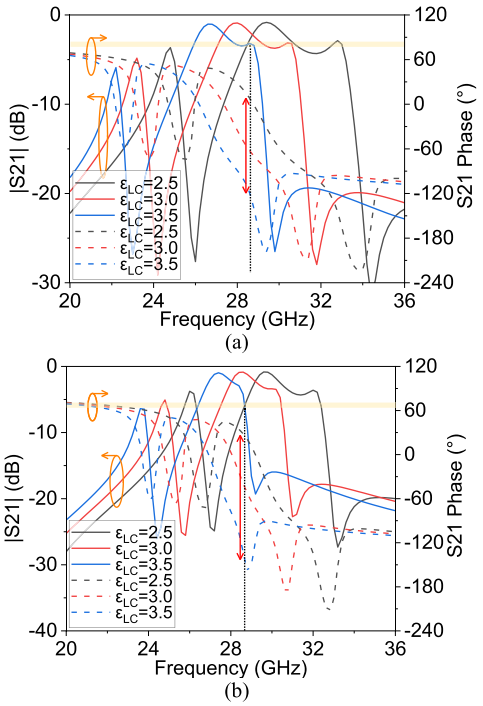

Fig. 8. Simulated S_{21} of the modified coupled resonator-loaded UCs with offset topology according to $\varepsilon_{\mathrm{LC}}$ with (a) 3 dB and (b) 6 dB losses for ST operation.

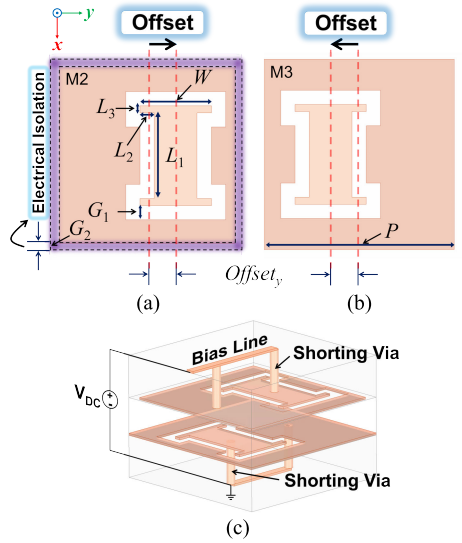

Fig. 9. Final configuration of the (a) top and (b) bottom resonators with their design parameters and (c) UC topology with biasing scheme.

TABLE I

DESIGN PARAMETERS AND THEIR VALUES IN FIG. 9

L_1	L_2	L_3	W	G_1	G_2	$Offset_y$	P
1.8	0.3	0.15	1.5	0.3	0.05	0.3	4

(Unit: mm)

adopted for optimized transmissive characteristics in the operating band with reasonable bandwidth. Fig. 9(c) shows the final UC topology with the dc biasing scheme. The two separate parts of the M2 electrode were in contact with the upper bias line through individual metallic vias to increase the surface area of the dc electrode. This ensures the even induction of an electric field parallel

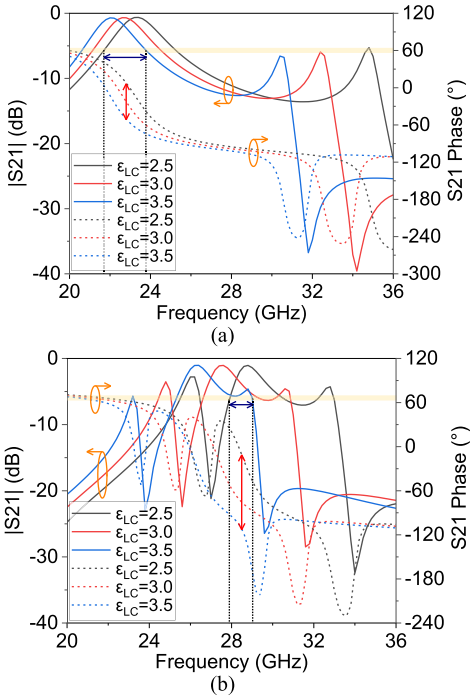

Fig. 10. Simulated S_{21} of the coupled resonator-loaded UCs of (a) non-offset and (b) offset topologies with biasing scheme according to ε_{LC}.

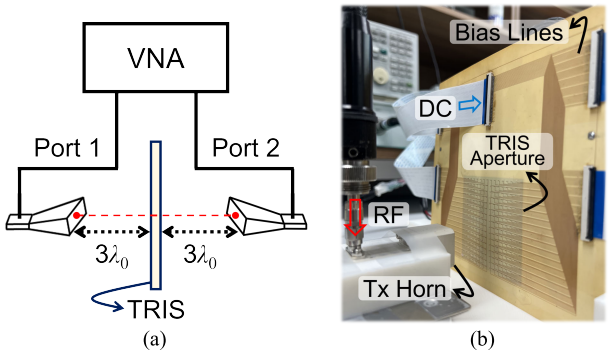

Fig. 11. Antenna measurement (a) schematic and (b) its photograph.

to the z-direction. The locations of the two vias in a complementary resonator have the lowest electric field intensity; therefore, the biasing scheme hardly deteriorates the S_{21} response of the optimally designed UC. The same electrical connection is also utilized for the M3 resonator as the dc GND, and the bias line extends in the y-direction to prevent the induction of current for x-polarized incident waves. Fig. 10 shows the simulated S_{21} of the coupled resonator-loaded UCs of non-offset and offset topologies with a biasing scheme according to ε_{LC}. Despite the drastic shift of the passband to a lower frequency due to the increase in ε_{LC}, the UC with an offset topology successfully achieves an operating band of 27.9–29 GHz with a PTR of 100°–123°, as shown in Fig. 10(b). In contrast, the UC with a non-offset topology operates with two independent resonant frequencies, functioning as dual bands. Therefore, the operating band around 23 GHz achieves a decreased narrow PTR of less than 58°.

Fig. 11 shows the antenna measurement schematic and its photograph. A 16 × 16 TRIS ($6 \times 6\lambda_0^2$ at 28 GHz) is fabricated to measure the transmissive characteristics of the proposed UC using the free-space method. The TRx antennas are standard horns operating in the Ka-band with a gain of 13 dBi at 28 GHz. The distance

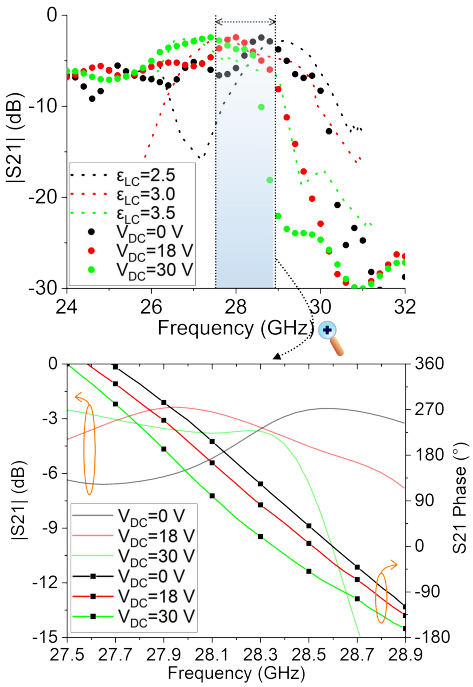

Fig. 12. Simulated and measured S_{21} of the fabricated TRIS by the free-space method with wide and narrow frequency spans.

between TRx and TRIS is $3\lambda_0$ within the radiating near-field region of the horn. The distance at which the majority of the power is illuminated inside the aperture is chosen to mitigate unintentional scattering caused by bias lines and flat flexible cables located outside the TRIS aperture. DC voltages were applied to 256 individual bias lines using the control board. In this experiment, identical voltage values were simultaneously applied to all electrodes to extract the UC parameters. Fig. 12 shows the simulated and measured S_{21} of the fabricated TRIS by the free-space method. The dotted line represents the simulated results of the TRIS aperture without bias lines for ε_{LC}, while the circular scatterer corresponds to the measured results for dc voltage. As shown in the upper figure, the passbands move to lower frequencies as ε_{LC} and dc voltage increase. Notably, the out-of-band rejection for the higher-frequency band of measured results is significantly enhanced compared to that of the simulated results. This is estimated by the use of bias lines arranged perpendicular to the x-polarized incident electric field, which is modeled as a shunt capacitor. As shown in the lower figure, the measured operating band ranges from 27.9 to 28.5 GHz, with a corresponding PTR of 92°–110°. Minor measurement errors can be attributed to several factors. These include limitations in modeling only a portion of the TRIS without bias lines due to the computational burden, distortions in the incident angle of the UCs on the outer side of the TRIS aperture in the radiating near-field region, and an immature bonding process involving the perforated PCB, which has not yet been commercialized.

Table II shows a comparison between the proposed and prior LC-based transmissive UCs. The simulated operating band of previous studies is calculated based on the minimum values of simulated insertion losses that are commonly satisfied for all LC dielectric constant values in each study. These values are equal to the respective maximum values in the simulated insertion loss column of Table II. Prior mmWave studies [6] and [7] achieved a relatively wide PTR, but did not report experimental results because the dual-layered LC with

TABLE II
COMPARISON BETWEEN THE PROPOSED AND PRIOR LC-BASED UCS

Ref	Freq (GHz)	LC Cell Gap (mm)	Number of LC Layer	Simulated Operating Band (GHz)	Simulated Insertion Loss (dB)	Simulated Maximum PTR (°)	Measured Maximum PTR (°)
[6]	340	0.58	2	300 – 400	0 – 5	180	N/A
[7]	27.4	0.762	2	N/A	2 – 9	170	N/A
[8]	30.4	0.015	1	30.4 (ST)	1.6 – 7.7	60	N/A
[9]	28.8	N/A	1	28.8 (ST)	2 – 4.5	N/A	N/A
[16]	133	0.13	1	133 (ST)	2.5 – 4.5	N/A	N/A
[17]	1000	0.250	1	N/A	N/A	86	N/A
[18]	387	0.064	1	384.5 – 388	13.5 – 17	374.1	175.3
[19]	408	0.06	1	408 (ST)	3 – 6	180	N/A
This Work	29	0.21	1	27.9 – 29	1.2 – 6	123	110

a thickened cell gap is difficult to fabricate and cannot be controlled with practical values of dc voltage. In [8], a single-layered LC with a slimmed cell gap was utilized, but a limited PTR of 60° was reported. Moreover, UCs in [16], [17], [18], and [19] were optimized with moderate values of cell gap, thanks to the reduction in physical dimensions due to increasing frequencies up to sub-THz. However, most of them maintained low loss only for STs. Among them, the UC in [18], which reported a reasonable bandwidth and a widened PTR, achieved a substantial level of loss. On the other hand, the proposed UC successfully achieves an improved PTR of more than twofold along with lower insertion loss in a rational bandwidth compared to its mmWave counterpart, utilizing a single-layered slimmed cell gap that is reasonably controllable.

III. CONCLUSION

This communication proposes an intriguing methodology for designing transmissive UCs using a single-layered LC, achieved by electromagnetically tailoring the effective cell gap to attain a slimmed and fully controllable topology. A coupled resonator-loaded UC is introduced, wherein the LC is sandwiched, adopting a dumbbell-shaped complementary topology to enhance its transmissive properties. Additionally, an innovative asymmetrical offset configuration is employed to increase the effective cell gap, surpassing the less desirable method of physically increasing the cell gap. This design enhances LC controllability in the mmWave band but requires improvements to address limitations related to angular stability due to its asymmetry and single-polarization operation. Nonetheless, this study introduces diverse scientific avenues for RIS research, which currently exhibits bias toward reflective types, and offers valuable insights for the advancement of more sophisticated transmissive UCs. These advancements will be explored in future endeavors, with a focus on high value-added 5G outdoor-to-indoor communication scenarios.

REFERENCES

[1] H. Kim, J. Kim, and J. Oh, "Liquid-crystal-based X-band reactively loaded reflectarray unit cell to reduce reflection loss," *IEEE Antennas Wireless Propag. Lett.*, vol. 20, no. 10, pp. 1898–1902, Oct. 2021.

[2] X. Li et al., "Broadband electronically scanned reflectarray antenna with liquid crystals," *IEEE Antennas Wireless Propag. Lett.*, vol. 20, no. 3, pp. 396–400, Mar. 2021.

[3] W. Zhang, Y. Li, and Z. Zhang, "A reconfigurable reflectarray antenna with an 8 μm-thick layer of liquid crystal," *IEEE Trans. Antennas Propag.*, vol. 70, no. 4, pp. 2770–2778, Apr. 2022.

[4] G. Perez-Palomino et al., "Design and demonstration of an electronically scanned reflectarray antenna at 100 GHz using multiresonant cells based on liquid crystals," *IEEE Trans. Antennas Propag.*, vol. 63, no. 8, pp. 3722–3727, Aug. 2015.

[5] W. Hu et al., "Design and measurement of reconfigurable millimeter wave reflectarray cells with nematic liquid crystal," *IEEE Trans. Antennas Propag.*, vol. 56, no. 10, pp. 3112–3117, Oct. 2008.

[6] X. Li, Z. Li, C. Wan, and S. Song, "Design and analysis of terahertz transmitarray using 1-bit liquid crystal phase shifter," in *Proc. 9th Asia–Pacific Conf. Antennas Propag. (APCAP)*, Xiamen, China, Aug. 2020, pp. 1–2.

[7] M. Maasch, M. Roig, C. Damm, and R. Jakoby, "Voltage-tunable artificial gradient-index lens based on a liquid crystal loaded fish-net metamaterial," *IEEE Antennas Wireless Propag. Lett.*, vol. 13, pp. 1581–1584, 2014.

[8] P.-Y. Wang et al., "A liquid crystal tunable metamaterial unit cell for dynamic metasurface antennas," *IEEE Trans. Antennas Propag.*, vol. 71, no. 1, pp. 1135–1140, Jan. 2023.

[9] P.-Y. Wang, A. Rennings, and D. Erni, "A liquid crystal based dynamic metasurface for beam steering and computational imaging," in *Proc. IEEE Asia–Pacific Microw. Conf. (APMC)*, Dec. 2020, pp. 631–633.

[10] J. Kim and J. Oh, "Liquid-crystal-embedded aperture-coupled microstrip antenna for 5G applications," *IEEE Antennas Wireless Propag. Lett.*, vol. 19, no. 11, pp. 1958–1962, Nov. 2020.

[11] J. Kim, W. Lee, and J. Oh, "Liquid-crystal-tuned resonant series patch array with unique element spacing emulating simplified operating construe of traveling-wave antenna," *IEEE Antennas Wireless Propag. Lett.*, Aug. 2023.

[12] M. Nestoros, N. C. Papanicolaou, and A. C. Polycarpou, "Design of beam-steerable array for 5G applications using tunable liquid-crystal phase shifters," in *Proc. 13th Eur. Conf. Antennas Propag. (EuCAP)*, Mar. 2019, pp. 1–4.

[13] C. D. Woehrle, D. T. Doyle, S. A. Lane, and C. G. Christodoulou, "Space radiation environment testing of liquid crystal phase shifter devices," *IEEE Antennas Wireless Propag. Lett.*, vol. 15, pp. 1923–1926, 2016.

[14] B.-J. Che, T. Jin, D. Erni, F.-Y. Meng, Y.-L. Lyu, and Q. Wu, "Electrically controllable composite right/left-handed leaky-wave antenna using liquid crystals in PCB technology," *IEEE Trans. Compon., Packag., Manuf. Technol.*, vol. 7, no. 8, pp. 1331–1342, Aug. 2017.

[15] A. E. Prasetiadi et al., "Electrical biasing scheme for liquid-crystal-based tunable substrate integrated waveguide structures," in *Proc. German Microw. Conf. (GeMiC)*, Bochum, Germany, Mar. 2016, pp. 136–139.

[16] W. Hu et al., "Liquid crystal tunable mm-wave frequency selective surface," *IEEE Microw. Wireless Compon. Lett.*, vol. 17, no. 9, pp. 667–669, Sep. 2007.

[17] Y. Shen, Z. Shen, Y. Wang, D. Xu, and W. Hu, "Electrically tunable terahertz focusing modulator enabled by liquid crystal integrated dielectric metasurface," *Crystals*, vol. 11, no. 5, p. 514, May 2021.

[18] J. Yang et al., "Rapid terahertz wave manipulation in a liquid-crystal-integrated metasurface structure," *Opt. Exp.*, vol. 30, no. 18, p. 33014, Aug. 2022.

[19] C. X. Liu et al., "Programmable manipulations of terahertz beams by transmissive digital coding metasurfaces based on liquid crystals," *Adv. Opt. Mater.*, vol. 9, no. 22, Nov. 2021, Art. no. 2100932.

[20] X.-D. Hu, X.-L. Zhou, L.-S. Wu, L. Zhou, and W.-Y. Yin, "A miniaturized dual-band frequency selective surface (FSS) with closed loop and its complementary pattern," *IEEE Antennas Wireless Propag. Lett.*, vol. 8, pp. 1374–1377, 2009.

[21] A. H. Abdelrahman, F. Yang, A. Z. Elsherbeni, P. Nayeri, and P. Nayeri, *Analysis and Design of Transmitarray Antennas*. San Francisco, CA, USA: Morgan & Claypool, 2017.

[22] J.-S. Hong and M. J. Lancaster, "Couplings of microstrip square open-loop resonators for cross-coupled planar microwave filters," *IEEE Trans. Microw. Theory Techn.*, vol. 44, no. 11, pp. 2099–2109, Nov. 1996.

[23] K. Ma, J.-G. Ma, K. Seng Yeo, and M. Anh Do, "A compact size coupling controllable filter with separate electric and magnetic coupling paths," *IEEE Trans. Microw. Theory Techn.*, vol. 54, no. 3, pp. 1113–1119, Mar. 2006.

[24] J.-S. Hong and M. J. Lancaster, "Aperture-coupled microstrip open-loop resonators and their applications to the design of novel microstrip bandpass filters," *IEEE Trans. Microw. Theory Techn.*, vol. 47, no. 9, pp. 1848–1855, Sep. 1999.